Available online at www.sciencedirect.com
SCIENCE DIRECT®
Journal of Computational Physics 203 (2005) 22–48
JOURNAL OF COMPUTATIONAL PHYSICS
www.elsevier.com/locate/jcp

A compressible finite volume formulation for large eddy simulation of turbulent pipe flows at low Mach number in Cartesian coordinates

Xiaofeng Xu [a,*], Joon Sang Lee [a,1], Richard H Pletcher [b]

[a] Department of Mechanical Engineering, 2025 Black Engineering Building, Iowa State University, Ames, IA 50011, USA
[b] Department of Mechanical Engineering, 3024 Black Engineering Building, Iowa State University, Ames, IA 50011, USA

Received 31 March 2003; received in revised form 28 June 2004; accepted 3 August 2004
Available online 16 September 2004

Abstract

A finite volume formulation for large eddy simulation (LES) of turbulent pipe flows based on the compressible time-dependent three-dimensional Navier–Stokes equations in Cartesian coordinates with non-Cartesian control volumes is presented. The small scale motions are modeled by a dynamic subgrid-scale (SGS) model. A dual-time stepping approach with time derivative preconditioning is employed to enable the simulations to run efficiently at low Mach numbers. The equations with primitive variables, (p, u, v, w, T), are solved with an implicit lower-upper-symmetric-Gauss–Seidel (LU-SGS) scheme. An isothermal turbulent pipe flow at two Reynolds numbers, and a turbulent pipe flow with a low heat transfer are simulated to evaluate this compressible LES finite volume formulation. The results agree very well with the experimental data and DNS results, verifying the accuracy of the present scheme.

Keywords: Large eddy simulation; Finite volume formulation; Compressible Navier–Stokes equations; Low Mach number

1. Introduction

As computer hardware and algorithms improve, increasing attention is being given to direct numerical simulation (DNS) and large eddy simulation (LES) of turbulent flows to obtain more accurate results, par-

* Corresponding author. Present address: Department of Mechanical engineering, The Johns Hopkins University, 3400 North Charles Street, Baltimore, MD 21218, USA. Tel.: +410 516 6780; fax: +410 516 4316.
E-mail address: xxf@iastate.edu (X. Xu).
[1] Present address: Department of Mechanical Engineering, Wayne State University, 5050 Anthony Wayne Drive, Rm 2100, Detroit, MI 48202, USA.

0021-9991/$ - see front matter © 2004 Elsevier Inc. All rights reserved.
doi:10.1016/j.jcp.2004.08.005

ticularly at low Reynolds numbers. Most DNS and LES studies have been for planar channel flows and the simulations for flows in circular tubes are very sparse, especially with the compressible Navier–Stokes equations.

Eggels et al. [1] performed DNS computations for fully developed incompressible pipe flow with an finite volume formulation in cylindrical coordinates at low Reynolds number. An extended grid volume at the axis was needed in the radial momentum equation to avoid the singularity at the center line of the pipe. Orlandi and Fatica [2] simulated a rotating pipe flow with a finite difference approach in cylindrical coordinates. The singularity was avoided by using the radial flux on a staggered grid. Based on the same idea, Satake and Kunugi [3] have developed a finite volume scheme without a singularity for DNS of turbulent pipe flows. Using the same approach, Satake and Kunugi [4] successfully simulated an axisymmetric impinging jet with outflow confined between two parallel discs. This approach was further extended by involving the energy equation to predict flows in circular tubes with three thermal boundary conditions: uniform heat flux, a cosine distribution and circumferential non-uniform wall temperature [5]. DNS of turbulent heat transfer in an axially rotating pipe flow with uniform heat flux was also performed by Satake and Kunugi [6].

The LES work for turbulent pipe flow is very limited. To the authors' knowledge, the first LES of fully developed incompressible turbulent pipe flow was computed by Unger and Friedrich [7]. Eggels and Nieuwstadt [8] simulated rotating pipe turbulent flow by LES using a finite volume formulation with a Smagorinsky subgrid-scale model. LES of turbulent flow in a curved pipe was reported by Boersma and Nieuwstadt [9], and recently a dynamic subgrid-scale model has been used by Yang [10] to simulate fully developed turbulent rotating pipe flow. All of these investigations solved the conserve equations represented in the cylindrical coordinate system.

It should be noted that the incompressible Navier–Stokes equations were employed in the above simulations including simulations with heat transfer, where the passive scalar approach was employed. Recently, Satake et al. [11] performed DNS for a turbulent gas flow using the compressible Navier–Stokes equations with variable gas properties to grasp and understand the laminarization phenomena caused by strong heating. To the authors' knowledge, no LES work has been reported that used a compressible finite volume formulation to allow property variations for turbulent pipe flow. It is important and of interest to develop a suitable finite volume formulation for LES to simulate turbulent pipe flows with significant property variations.

The objective of the present study was to develop an efficient colocated finite volume scheme for flows in tubes and annuli based on the compressible three-dimensional Navier–Stokes equations along with the compressible continuity and energy equations in Cartesian coordinates. The purpose of using a compressible formulation is to enable simulations for which the temperature variation within the flow is very significant. However, in the present paper, results are limited to low heat transfer cases to enable comparisons with results based on treating the temperature as a passive scalar. Non-Cartesian hexahedral and tetrahedral control volumes constructed in cylindrical coordinates were used. The equations were solved for the primitive variables (p, u, v, w, T) using a low Mach number preconditioned [12] implicit lower-upper-symmetric-Gauss–Seidel (LU-SGS) scheme [13] that is second-order accurate in space and time. The method and rationale for using the equations in Cartesian coordinates will be discussed in the sections to follow. Simulation results for turbulent pipe flows with and without heat transfer are compared with experimental data and DNS results.

2. Governing equations for LES

For gas flows in a tube with property variations (density, viscosity, and conductivity) in the axial and radius directions, the compressible Navier–Stokes equations are applicable even if a low speed case

is treated. The effects of the smallest scale motions were separated from large scale motions by using the top-hat filter function, which is defined as

$$G(\vec{x},\vec{\xi}) = \begin{cases} 1/\Delta^3, & |x_i - \xi_i| \leqslant \Delta/2 \quad (i = 1,2,3), \\ 0, & |x_i - \xi_i| > \Delta/2, \end{cases} \tag{1}$$

where Δ is the filter width. In this paper, $V^{1/3}$ was used as the filter width where V is the volume of the control volume.

The filtering operation does not generally commute with the differentiation operation for LES of inhomogeneous turbulent flow with a variable filter width. The commutation error is second-order in the filter width [15]. In this work, since the grid spacing is the same order as the filter width and a second-order numerical scheme is used, the finite difference error is then the same order as the commutation error. Therefore, the present filtering operation can be considered to commute with the differentiation operation within the accuracy of the numerical approximation. To avoid the numerical contamination due to commutation error, the grid space is uniform in streamwise and circumferential directions, and smoothly varying in the radial direction, the maximum stretching ratio is 1.07.

Farve-filtering [16] was used to simplify the filtered equations for compressible flow and yielded the Favre-filtered non-dimensional compressible Navier–Stokes equations

$$\frac{\partial \overline{\rho}}{\partial t} + \frac{\partial(\overline{\rho}\tilde{u}_j)}{\partial x_j} = 0, \tag{2}$$

$$\frac{\partial(\overline{\rho}\tilde{u}_i)}{\partial t} + \frac{\partial(\overline{\rho}\tilde{u}_i\tilde{u}_j)}{\partial x_j} = -\frac{\partial \overline{p}}{\partial x_i} + \frac{\partial \overline{\sigma}_{ij}}{\partial x_j} - \frac{\partial \tau_{ij}}{\partial x_j}, \tag{3}$$

$$\frac{\partial(\overline{\rho}\hat{E})}{\partial t} + \frac{\partial[(\overline{\rho}\hat{E} + \overline{p})\tilde{u}_j]}{\partial x_j} = \frac{\partial(\tilde{u}_i\bar{\sigma}_{ij})}{\partial x_j} - \frac{\partial \bar{q}_j}{\partial x_j} - \frac{\partial Q_j}{\partial x_j} - \alpha - \pi - \varepsilon, \tag{4}$$

and the equation of state

$$\overline{p} = R\overline{\rho}\tilde{T}. \tag{5}$$

The effects of the small-scale motions are present in the above equations through the subgrid-scale (SGS) stress tensor, τ_{ij}, in the momentum equation as

$$\tau_{ij} = \overline{\rho}(\widetilde{u_i u_j} - \tilde{u}_i\tilde{u}_j), \tag{6}$$

and the SGS terms that are the last four terms on the right hand side of Eq. (4) (energy equation) as

$$Q_j = \overline{\rho}c_v(\widetilde{Tu_j} - \tilde{T}\tilde{u}_j), \tag{7}$$

$$\alpha = \tilde{u}_i\frac{\partial \tau_{ij}}{\partial x_j}, \tag{8}$$

$$\pi = \overline{p\frac{\partial u_j}{\partial x_j}} - \overline{p}\frac{\partial \tilde{u}_j}{\partial x_j}, \tag{9}$$

$$\varepsilon = \overline{\sigma_{ij}\frac{\partial u_i}{\partial x_j}} - \hat{\sigma}_{ij}\frac{\partial \tilde{u}_j}{\partial x_j}, \tag{10}$$

where Q_j is the SGS heat flux vector. For the present work, it is appropriate to neglect α, π and ε since only low Mach number flows were considered [17].

The advantages of solving the conservation equations resolved in the Cartesian coordinate system include the following. First, the Cartesian based equations are as simple as possible and can be put in strong conservation (or divergence) form, which generally helps toward maintaining accuracy. If the alternative coordinate-oriented systems such as the cylindrical or polar systems are used, the basis vectors change directions, which introduces an "apparent force" to cause the turning that is non-conservative in form and hard to represent accurately. Second, the equations in the cylindrical and polar systems contain singularities at the coordinate origin. It is true that grid-related singularities may also occur when the Cartesian-based equations are used, but these are usually easier to accommodate than singularities in the equations themselves. It is generally accepted that there is no advantage to using equations represented in the cylindrical or polar coordinate systems for numerical computations if the flows are three-dimensional in nature [14].

To close the system of equations, the SGS stress tensor and heat flux vector in the Favre-filtered equations need to be modeled. In this paper, the dynamic model proposed for compressible turbulence by Moin et al. [18] and recommended by Lilly [19] was implemented. The test filter width is defined in the same way as the grid filter width and is equal to twice the grid filter width.

3. Finite volume formulation

A coupled finite volume method was used to solve the filtered compressible Navier–Stokes equations based on Cartesian coordinates. This approach has been successfully tested on planar channel flow with Cartesian hexahedral control volumes [13]. The finite volume formulation used here is valid for pipe flows with non-Cartesian control volumes.

3.1. Computational domain

As shown in Fig. 1, the computational domain is cut along the radius *oa*, and points *a* and *b* are the same point. Consequently, the computational domain has four boundaries, boundary *oa*, boundary *ob*, boundary *ab* and point *o*. Periodic boundary conditions are applied on the boundaries of *oa* and *ob* which are actually the same boundary, no slip boundary conditions are used on the wall boundary, *ab*. For point *o*, no boundary condition is needed because the area goes zero and the momentum and mass fluxes are zero also. Consequently, no singularity is encountered at the center point.

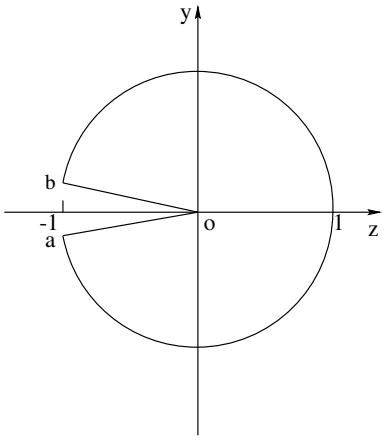

Fig. 1. Sketch of the cross-section of the computational domain.

3.2. Integral approximation

The solution domain was continuously subdivided into non-Cartesian hexahedral and tetrahedral control volumes of unequal dimensions based on cylindrical coordinates. The typical two types of control volumes are shown in Fig. 2. The primitive variables $(\bar{p}, \tilde{u}_i, \tilde{T})$ were stored at the geometric centers of the control volumes (cell center scheme). With the cell center approach, the solution domain is easier to decompose into multiple blocks. That is very important for the treatment of complex geometries and parallelization of the code.

The volume integral can be approximated by the product of the mean value and the volume of the cell, and the mean value can be approximated as the value at the center of the control volume. To calculate the surface integral exactly, the flux vectors should be known everywhere on the surface. Since the information at the center of the control volumes are available, the cell face values can be approximated in terms of the volume center values using the "mid-point" rule. A weighting function is needed to interpolate the volume center values at cell faces in the radial direction because the grid is stretched toward the wall. Consequently, the surface integrals can be approximated as

$$\int_{\partial\Omega} (\mathbf{E}\vec{i} + \mathbf{F}\vec{j} + \mathbf{G}\vec{k}) \cdot \mathrm{d}\vec{S} \approx \sum_{\beta=1}^{6} [(\mathbf{E}n_x + \mathbf{F}n_y + \mathbf{G}n_z)S]_{\beta}, \tag{11}$$

where $\boldsymbol{E}$, $\boldsymbol{F}$ and $\boldsymbol{G}$ are the flux vectors in the x, y and z directions, respectively. The vector, $\mathrm{d}\vec{S}$, is the cell face area vector and (n_x, n_y, n_z) is the unit normal of the cell face. For the cell faces in the streamwise and circumferential directions, S is the magnitude of the face area vector, but for the cell faces in the radial direction, S is the area of the projected-surface which is constructed by projecting the curved cell face onto a plane perpendicular to (n_x, n_y, n_z).

The gradients of velocity components and the temperature are needed at the cell faces to calculate the viscous and sub-grid scale contributions to the flux vectors. The gradients were calculated using the Gauss divergence theorem on an auxiliary control volume as

$$\int_{\Omega'} \nabla\phi \, \mathrm{d}\Omega' = \int_{\partial\Omega'} \phi \, \mathrm{d}\vec{S}', \tag{12}$$

where ϕ is a scalar, Ω' is the volume of auxiliary control volume and $\mathrm{d}\vec{S}'$ is the cell face area vector of the auxiliary volume. The auxiliary control volume was obtained by shifting the main control volume a half index in the direction of the particular cell face on which the gradient was to be calculated.

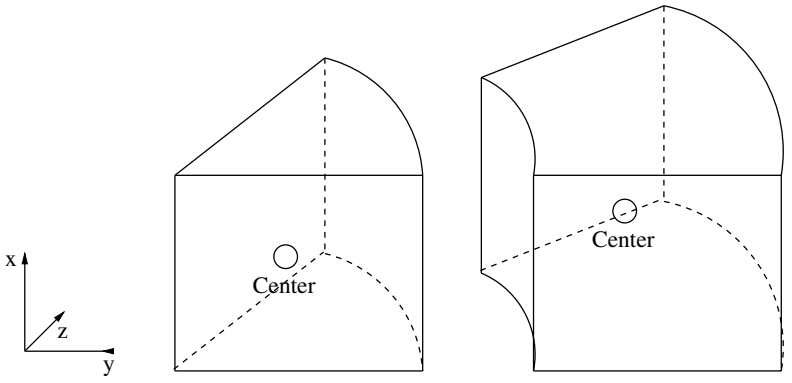

Fig. 2. Sketch of control volumes.

Time-derivative preconditioning [12] has been used to enable the computation of low Mach number flows. The addition of the pseudo time derivative is termed the dual time step approach, and involves iterating in pseudo time for each step in physical time. The original unsteady governing equations were satisfied when the iteration process converged in pseudo time. The pseudo time derivative was discretized with a first-order accurate Euler backward difference, and the physical time derivative was discretized with a second-order accurate three-point backward difference. Time integration was performed using the implicit LU-SGS scheme which will be discussed next.

3.3. LU-SGS scheme

The preconditioned, time accurate Favre-filtered governing equations were linearized about pseudo time level m as

$$\left\{\frac{\Omega}{\Delta\tau}[I]+[\Gamma]^{-1}[T]\frac{3}{2}\frac{\Omega}{\Delta t}+[\Gamma]^{-1}\sum_{\beta=1}^{6}[([A]_{nx}+[B]_{ny}+[C]_{nz})S]_{\beta}\right\}^{m}\Delta\boldsymbol{W}=-\Re^{m}, \tag{13}$$

where $[\Gamma]$ is the preconditioning matrix, $[A]$, $[B]$ and $[C]$ are linearized inviscid flux vectors in x, y and z directions, respectively. $\boldsymbol{W}$ is the vector of primitive variables and $\Re$ is the preconditioned residual. The viscous stresses and sub-grid scale stresses were lagged as the values of the previous pseudo time step and included in the preconditioned residual. The surface index is defined as shown in Fig. 3 and we define the surfaces in the streamwise direction as surfaces 1 and 3. The inviscid flux Jacobians on each face are defined as

$$\begin{aligned}
[\hat{A}] &= ([A])_{\beta=1,3},\\
[\hat{B}] &= ([B]n_{1_y}+[C]n_{1_z})_{\beta=2,4},\\
[\hat{C}] &= ([B]n_{2_y}+[C]n_{2_z})_{\beta=5,6}.
\end{aligned} \tag{14}$$

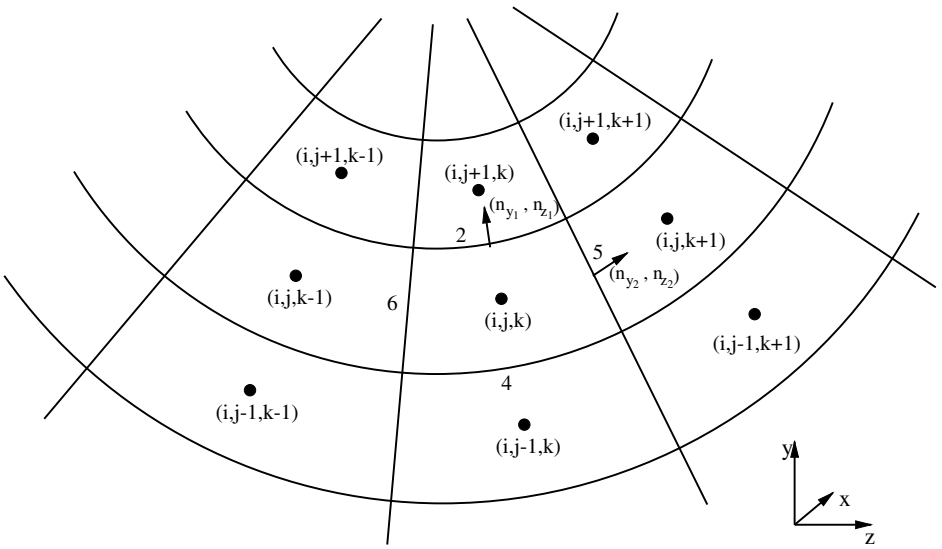

Fig. 3. Sketch of grid representation in yz plane.

Substituting inviscid flux Jacobians by using Eq. (14), the linearized equation, Eq. (13), can be written as

$$\left\{\frac{\Omega}{\Delta\tau}[I]+[\Gamma]^{-1}[T]\frac{3}{2}\frac{\Omega}{\Delta t}+[\Gamma]^{-1}[[\hat{A}]_1S_1-[\hat{A}]_3S_3+[\hat{B}]_2S_2-[\hat{B}]_4S_4+[\hat{C}]_5S_5-[\hat{C}]_6S_6]\right\}\Delta\boldsymbol{W}=-\Re. \quad (15)$$

The pseudo-time step, $\Delta\tau$, was set to infinity, corresponding to a Newton iteration that drives the Newton linearization error to zero in each physical time step.

The flux Jacobians were modified [20] to accommodate the preconditioning matrix as

$$[\tilde{A}]=[\Gamma]^{-1}[\hat{A}],\quad [\tilde{B}]=[\Gamma]^{-1}[\hat{B}],\quad [\tilde{C}]=[\Gamma]^{-1}[\hat{C}]. \quad (16)$$

The flux Jacobians were split as

$$[\tilde{A}]=[\tilde{A}]^{+}+[\tilde{A}]^{-},\quad [\tilde{B}]=[\tilde{B}]^{+}+[\tilde{B}]^{-},\quad [\tilde{C}]=[\tilde{C}]^{+}+[\tilde{C}]^{-}. \quad (17)$$

where

$$\begin{aligned}[\tilde{A}]^{\pm}&=\frac{1}{2}([\tilde{A}]\pm|\lambda_{[\tilde{A}]}|[I]),\\ [\tilde{B}]^{\pm}&=\frac{1}{2}([\tilde{B}]\pm|\lambda_{[\tilde{B}]}|[I]),\\ [\tilde{C}]^{\pm}&=\frac{1}{2}([\tilde{C}]\pm|\lambda_{[\tilde{C}]}|[I]).\end{aligned} \quad (18)$$

The quantities $\lambda_{[\tilde{A}]}$, $\lambda_{[\tilde{B}]}$ and $\lambda_{[\tilde{C}]}$ are the maximum eigenvalues of the flux Jacobians $[\tilde{A}]$, $[\tilde{B}]$ and $[\tilde{C}]$, respectively. For the preconditioned system, the maximum eigenvalues are

$$\begin{aligned}\lambda_{[\tilde{A}]}&=\frac{1}{2R}\left[(R+1)|\tilde{u}|+\sqrt{(R-1)^2\tilde{u}^2+4Rc^2}\right],\\ \lambda_{[\tilde{B}]}&=\frac{1}{2R}\left[(R+1)|\tilde{v}n_{1_y}+\tilde{w}n_{1_z}|+\sqrt{(R-1)^2(\tilde{v}n_{1_y}+\tilde{w}n_{1_z})^2+4Rc^2}\right],\\ \lambda_{[\tilde{B}]}&=\frac{1}{2R}\left[(R+1)|\tilde{v}n_{2_y}+\tilde{w}n_{2_z}|+\sqrt{(R-1)^2(\tilde{v}n_{2_y}+\tilde{w}n_{2_z})^2+4Rc^2}\right],\end{aligned} \quad (19)$$

where R is the gas constant, c is the speed of sound and $\tilde{u}$, $\tilde{v}$ and $\tilde{w}$ are the Cartesian velocity components in the x, y and z directions, respectively.

The flux Jacobians on the control volume faces were approximated as

$$\begin{aligned}([\Gamma][\tilde{A}]\Delta W)_1S_1&=([\Gamma][\tilde{A}]^{+}\Delta W)_{i,j,k}S_1+([\Gamma][\tilde{A}]^{-}\Delta W)_{i+1,j,k}S_1,\\ ([\Gamma][\tilde{A}]\Delta W)_3S_3&=([\Gamma][\tilde{A}]^{+}\Delta W)_{i-1,j,k}S_3+([\Gamma][\tilde{A}]^{-}\Delta W)_{i,j,k}S_3,\\ ([\Gamma][\tilde{B}]\Delta W)_2S_2&=([\Gamma][\tilde{B}]^{+}\Delta W)_{i,j,k}S_{i,j,k}+([\Gamma][\tilde{B}]^{-}\Delta W)_{i,j+1,k}S_{i,j+1,k},\\ ([\Gamma][\tilde{B}]\Delta W)_4S_4&=([\Gamma][\tilde{B}]^{+}\Delta W)_{i,j-1,k}S_{i,j-1,k}+([\Gamma][\tilde{B}]^{-}\Delta W)_{i,j,k}S_{i,j,k},\\ ([\Gamma][\tilde{C}]\Delta W)_5S_5&=([\Gamma][\tilde{C}]^{+}\Delta W)_{i,j,k}S_5+([\Gamma][\tilde{C}]^{-}\Delta W)_{i,j,k+1}S_5,\\ ([\Gamma][\tilde{C}]\Delta W)_6S_6&=([\Gamma][\tilde{C}]^{+}\Delta W)_{i,j,k-1}S_6+([\Gamma][\tilde{C}]^{-}\Delta W)_{i,j,k}S_6,\end{aligned} \quad (20)$$

where $S_1=S_2$, $S_5=S_6$ and $S_{i,j,k}=1/2(S_2+S_4)_{i,j,k}$.

After substituting Eqs. (16) and (20) into Eq. (15) the result can be written as

$$([L]+[D]+[U])\Delta\boldsymbol{W}=-\Re, \quad (21)$$

where the matrices $[L]$, $[D]$ and $[U]$ are

$$[L]=-[\Gamma]^{-1}[([\Gamma][\tilde{A}]^{+})_{i-1,j,k}S_3+([\Gamma][\tilde{B}]^{+})_{i,j-1,k}S_{i,j-1,k}+([\Gamma][\tilde{C}]^{+})_{i,j,k-1}S_6], \quad (22)$$

$$[D] = [\Gamma]^{-1}[T]\frac{3}{2}\frac{\Omega}{\Delta t} + [\Gamma]^{-1}[([\Gamma][\tilde{A}]^{+})_{i,j,k}S_1 - ([\Gamma][\tilde{A}]^{-})_{i,j,k}S_3 + ([\Gamma][\tilde{B}]^{+})_{i,j,k}S_{i,j,k} - ([\Gamma][\tilde{B}]^{-})_{i,j,k}S_{i,j,k} + ([\Gamma][\tilde{C}]^{+})_{i,j,k}S_5 - ([\Gamma][\tilde{C}]^{-})_{i,j,k}S_6], \tag{23}$$

$$[U] = [\Gamma]^{-1}[([\Gamma][\tilde{A}]^{-})_{i+1,j,k}S_1 + ([\Gamma][\tilde{B}]^{-})_{i,j+1,k}S_{i,j+1,k} + ([\Gamma][\tilde{C}]^{-})_{i,j,k+1}S_5]. \tag{24}$$

Because of the splitting of the flux Jacobians,

$$[\Gamma][\tilde{A}]^{+} - [\Gamma][\tilde{A}]^{+} = |\lambda_{[\tilde{A}]}|, \tag{25}$$

$$[\Gamma][\tilde{B}]^{+} - [\Gamma][\tilde{B}]^{+} = |\lambda_{[\tilde{B}]}|, \tag{26}$$

$$[\Gamma][\tilde{C}]^{+} - [\Gamma][\tilde{C}]^{+} = |\lambda_{[\tilde{C}]}|, \tag{27}$$

the matrix $[D]$ can be reduced to

$$[D] = \frac{3}{2}\frac{\Omega}{\Delta t}[\Gamma]^{-1}[T] + (|\lambda_{[\tilde{A}]}|S_1 + |\lambda_{[\tilde{B}]}|S_{i,j,k} + |\lambda_{[\tilde{C}]}|S_5)[I]. \tag{28}$$

Because the product of $[\Gamma]^{-1}[T]$ is a diagonal matrix, the matrix $[D]$ is also diagonal. The north surface area, S_2, is zero in the central region and the matrices $[L]$, $[D]$ and $[U]$ were changed to

$$[L] = -[\Gamma]^{-1}[([\Gamma][\tilde{A}]^{+})_{i-1,j,k}S_3 + ([\Gamma][\tilde{B}]^{+})_{i,j-1,k}S_{i,j-1,k} + ([\Gamma][\tilde{C}]^{+})_{i,j,k-1}S_6], \tag{29}$$

$$[D] = [\Gamma]^{-1}[T]\frac{3}{2}\frac{\Omega}{\Delta t} + [\Gamma]^{-1}[([\Gamma][\tilde{A}]^{+})_{i,j,k}S_1 - ([\Gamma][\tilde{A}]^{-})_{i,j,k}S_3 - ([\Gamma][\tilde{B}]^{-})_{i,j,k}S_{i,j,k} + ([\Gamma][\tilde{C}]^{+})_{i,j,k}S_5 - ([\Gamma][\tilde{C}]^{-})_{i,j,k}S_6], \tag{30}$$

$$[U] = [\Gamma]^{-1}[([\Gamma][\tilde{A}]^{-})_{i+1,j,k}S_1 + ([\Gamma][\tilde{C}]^{-})_{i,j,k+1}S_5], \tag{31}$$

where the matrix $[D]$ can be simplified as

$$[D] = \frac{3}{2}\frac{\Omega}{\Delta t}[\Gamma]^{-1}[T] + (|\lambda_{[\tilde{A}]}|[I]S_1 - ([\Gamma][\tilde{B}]^{-})_{i,j,k}S_{i,j,k} + |\lambda_{[\tilde{C}]}|[I]S_5). \tag{32}$$

Eq. (21) can be approximately factored as

$$([L] + [D])[D]^{-1}([D] + [U])\Delta \boldsymbol{W} = -\Re, \tag{33}$$

and efficiently solved in three steps as follows:

$$\begin{aligned}
&\text{Step 1}: \quad ([L] + [D])\Delta \mathbf{W}^{*} = -\Re,\\
&\qquad\qquad \Delta \mathbf{W}^{*} = [D]^{-1}(-\Re - [L]\Delta \mathbf{W}^{*}),\\
&\text{Step 2}: \quad ([D] + [U])\Delta \mathbf{W} = [D]\Delta \mathbf{W}^{*},\\
&\qquad\qquad \Delta \mathbf{W} = \Delta \mathbf{W}^{*} - [D]^{-1}[U]\Delta \mathbf{W},\\
&\text{Step 3}: \quad \mathbf{W}^{m+1} = \mathbf{W}^{m} + \Delta \mathbf{W}.
\end{aligned}$$

Since $[D]$ is diagonal except for the control volumes in the center region, the inversion of $[D]$ required a trivial amount of work and hence the LU-SGS scheme was still very efficient compared to other implicit schemes.

4. Boundary conditions

Due to the cell center finite volume formulation, "ghost" or "image" cells, as depicted in Fig. 4, were needed to enforce the boundary conditions. The conditions lying on the boundaries were satisfied by setting up the proper values at ghost cells. Three boundary conditions used in this research are described here.

4.1. Solid wall boundary conditions

No slip boundary conditions were enforced for the velocity components at the solid walls as

$$\tilde{u}_g = -\tilde{u}_{nb}, \quad \tilde{v}_g = -\tilde{v}_{nb}, \quad \tilde{w}_g = -\tilde{w}_{nb}, \tag{34}$$

where the subscript 'g' denotes the ghost cell and the subscript 'nb' denotes the near wall control volume. Pressure was set as $\bar{p}_g = \bar{p}_{nb}$ by the approximate boundary condition $\partial\bar{p}/\partial n = 0$ at the solid wall.

For heat transfer cases, two ways of imposing the uniform heat flux wall boundary were applied: fixed wall temperature distribution and fixed wall heat flux. With fixed wall temperature distribution boundary condition, the temperature at ghost cells can be evaluated as $\tilde{T}_g = 2\tilde{T}_w - \tilde{T}_{nb}$. To enforce the fixed non-dimensional wall heat flux, q_w, at the wall, the temperature at the ghost cell was set as

$$\tilde{T}_g = \tilde{T}_{nb} + \frac{q_w RePr}{\mu_w}\Delta l, \tag{35}$$

where Δl is the distance between the cell centers of near the wall control volume and ghost cell and μ_w is the non-dimensional molecular viscosity at the wall. For variable property flows, the molecular viscosity at the wall is a nonlinear function of the wall temperature, $\mu_w = \mu_w(\tilde{T}_w)$. An iterative procedure is needed to obtain the correct viscosity value at the wall, and hence, ghost cell temperature. The non-dimensional heat flux is given in terms of the dimensional quantities as

$$q_w = \frac{q_w^*}{\rho_{ref} V_{ref} T_{ref} c_p^*}, \tag{36}$$

where the subscript, ref, denotes values at a reference state.

4.2. Periodic boundary conditions

For the isothermal cases considered in this research, the flows were assumed to be fully developed and they were simply assigned periodic boundary conditions at the inflow and outflow boundaries. The periodic

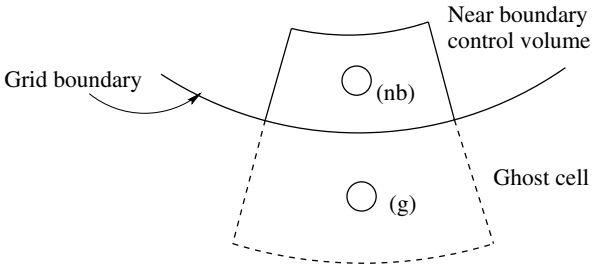

Fig. 4. Ghost cells for boundary conditions.

boundary conditions were enforced by copying values of the variables in the boundary control volume at the outflow boundary to the ghost cell at the inflow boundary, and by copying values of the variables in the boundary control volume at the inflow boundary to the ghost cell at the outflow boundary. The pressure actually is not periodic in the streamwise direction due to the negative, linear streamwise pressure gradient that drives the flow. The pressure was assumed to be step-periodic and decomposed into periodic and aperiodic components as

$$\bar{p}(x,y,z,t) = \beta x + \bar{p}_{\mathrm{p}}(x,y,z,t), \tag{37}$$

where β is the average streamwise pressure gradient. The equation of state becomes

$$\bar{\rho} = \frac{\bar{p}}{R\tilde{T}} = \frac{\beta x}{R\tilde{T}} + \frac{\bar{p}_{\mathrm{p}}}{R\tilde{T}}. \tag{38}$$

For moderate Reynolds numbers, the pressure gradient term is much smaller than the periodic pressure and $\beta x/(R\tilde{T})$ is negligible compared to $\bar{p}_{\mathrm{p}}/(R\tilde{T})$. Therefore, the density can be approximated as

$$\bar{\rho} \approx \frac{\bar{p}_{\mathrm{p}}}{R\tilde{T}}. \tag{39}$$

By replacing $\bar{p}$ with $\bar{p}_{\mathrm{p}}$ in the governing equation and adding the streamwise pressure gradient as a body force in the right hand side of the streamwise momentum equation, the periodic assumption for pressure can be satisfied and the periodic pressure component is determined in the simulation by requiring that the mean mass flow rate be constant. Following the approach investigated by Benocci and Pinelli [21], the average streamewise pressure gradient was calculated dynamically at each physical time step to provide the desired mass flow rate as

$$\beta^{n+1} = \beta^{n} - \frac{1}{\Delta t}\left[\left(\frac{\dot{m}}{A_{\mathrm{c}}}\right)^{0} - 2\left(\frac{\dot{m}}{A_{\mathrm{c}}}\right)^{n} + \left(\frac{\dot{m}}{A_{\mathrm{c}}}\right)^{n-1}\right], \tag{40}$$

where A_{c} is the cross-flow area of computational domain and Δt is the physical time step. The quantity $\dot{m}/A_{\mathrm{c}}$ is average mass flow rate and $(\dot{m}/A_{\mathrm{c}})^{0}$ is the desired mass flow rate. For example, the ghost cell values at the inflow boundary is set as

$$\begin{aligned}
\bar{p}_{\mathrm{g}} &= \bar{p}_{\mathrm{p}}(0,j,k) = \bar{p}_{\mathrm{p}}(ni,j,k),\\
\tilde{u}_{\mathrm{g}} &= \tilde{u}(0,j,k) = \tilde{u}(ni,j,k),\\
\tilde{v}_{\mathrm{g}} &= \tilde{v}(0,j,k) = \tilde{v}(ni,j,k),\\
\tilde{w}_{\mathrm{g}} &= \tilde{w}(0,j,k) = \tilde{w}(ni,j,k),\\
\tilde{T}_{\mathrm{g}} &= \tilde{T}(0,j,k) = \tilde{T}(ni,j,k).
\end{aligned} \tag{41}$$

Periodic boundary conditions were also enforced in the circumferential direction.

4.3. Step-periodic boundary conditions

For the heat transfer cases with property variations, due to the negative linear streamwise pressure gradient that drives the flow and the positive linear temperature gradient resulting from the heat addition, the periodicity assumptions were not valid for pressure, temperature or streamwise velocity. Step-periodic boundary conditions [13] were adopted in this work. This is implemented by assuming that the temperature variations in the streamwise direction are step-periodic for the uniform heat flux case and the local mass flux is streamwise-periodic. For example, the boundary conditions for the inlet boundary were given as

$$\begin{aligned}
\bar{p}_g &= \bar{p}_p(0,j,k) = \bar{p}_p(ni,j,k),\\
(\bar{\rho}\tilde{u})_g &= (\bar{\rho}\tilde{u})(0,j,k) = (\bar{\rho}\tilde{u})(ni,j,k),\\
\tilde{v}_g &= \tilde{v}(0,j,k) = \tilde{v}(ni,j,k),\\
\tilde{w}_g &= \tilde{w}(0,j,k) = \tilde{w}(ni,j,k),\\
\tilde{T}_g &= \tilde{T}(0,j,k) = \tilde{T}(ni,j,k) - \Delta\tilde{T}_x,
\end{aligned} \tag{42}$$

where $\Delta\tilde{T}_x$ is the average fluid temperature difference between inflow and outflow boundaries. When the heat transfer is low enough that the property variations are negligibly small, the value of $\Delta\tilde{T}_x$ can be approximated as the bulk temperature difference, ΔT_b, and fixed by the uniform heat flux boundary condition as

$$\Delta\tilde{T}_x = \frac{4q_w L}{(\dot{m}/A_c)D}, \tag{43}$$

where $\dot{m}/A_c$ is the non-dimensional mass flow rate per unit cross-sectional area, L is the non-dimensional length of computational domain, and D is the non-dimensional pipe diameter.

5. Results and discussion

5.1. Isothermal turbulent pipe flow

The simulation was designed to match the flow conditions of the available experimental and DNS results. The DNS computations were performed by Eggels et al. [1] with grid resolution $256 \times 96 \times 128$ in the streamwise, radial and circumferential directions, respectively. The laser Doppler anemometry (LDA) and particle image velocimetry (PIV) measurements were performed by Westerweel et al. [22]. The computational domain is shown in Fig. 5, where the radius of the pipe is denoted by r, and the length of the computational domain by L, where $L = 10r$. All the dimensions are normalized by the pipe radius r. The length of the computational domain, which should be long enough to include the largest scale structures, was chosen with the guidance of DNS simulations [1,7]. The target bulk Reynolds number based on hydraulic diameter was equal to 5300, the Mach number was 0.001, and the non-dimensional physical time step was 0.01. The simulations were run with eight processors on the Origin 2000 machines. For the simulation with fine grid resolution, $64 \times 40 \times 100$, it required about 5.6 CPU h for each processor per 1000 time steps.

To study the grid independence, simulations were performed with different grid resolutions. The results are shown here with $48 \times 32 \times 64$, $64 \times 40 \times 80$ and $64 \times 40 \times 100$ grids in the streamwise, radial and circumferential directions, respectively. Simulation with higher grid resolution, $96 \times 64 \times 128$, also has been con-

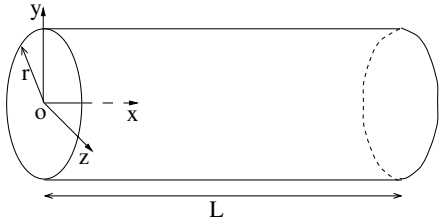

Fig. 5. Pipe flow geometry and coordinate system.

ducted, the results are very similar to that of grid resolution, $64 \times 40 \times 100$, as shown in Fig. 6. Therefore, the grid resolution, $64 \times 40 \times 100$, was used as the finest grid resolution for simulations at low Reynolds number in this paper. Grids were uniform in both the streamwise and circumferential directions, but clustered toward to the wall using the algebraic hyperbolic tangent stretching in the radial direction. The control volume dimensions in the streamwise and radial directions are given in Table 1 with respect to the radius and in wall coordinates. The superscript '+' represents a quantity in wall units, where in terms of non-dimensional variables, $x^+ = Re_{\mathrm{ref}} u_\tau x / \nu_{\mathrm{w}}$, where Re_{ref} is the reference Reynolds number and is defined as $Re_{\mathrm{ref}} = \rho_{\mathrm{ref}} u_{\mathrm{ref}} L_{\mathrm{ref}} / \mu_{\mathrm{ref}}$. The control volume dimension in the circumferential direction varied linearly with radius and the maximum and minimum spacings are given in Table 2. It was found that the grid resolution, $64 \times 40 \times 100$, was fine enough to solve the large scale field and the effect by refining the grid in the circumferential direction was more efficient for improving the accuracy than in the other two directions.

Some mean flow properties of the LES, DNS, and experiments are listed in Table 3, where u_{c} is the centerline velocity and u_{b} is the bulk velocity. As shown, the friction velocity, u_τ, of the two coarse grids is under-predicted, while the agreement between the results of the fine grid, DNS, and experimental results is within a few percent. The mean streamwise velocity profile normalized by friction velocity is shown in Fig. 6. The linear velocity distribution $u^+ = y^+$ for $y^+ < 5$ is well resolved with all the coarse and fine grids. For the region where $y^+ > 30$, the logarithmic velocity distribution represented by $u^+ = 2.5 \ln y^+ + 5.5$ is not followed exactly by the numerical simulations or experiments. Patel and Head [23] also observed that the flow in a pipe fails to conform to the accepted law of the wall even at Reynolds number considerably above 3000. Laufer [24] and Lawn [25] demonstrated that only for a Reynolds number much larger than the present one, does the turbulent pipe flow exhibit a logarithmic velocity distribution, at least in part of the cross section. However, the fine grid results agree very well with the DNS and experimental results. Large differences are observed between the results of both coarse grids and the DNS and experimental results.

The root-mean-square (rms) values of fluctuating velocities, normalized by the friction velocity, are shown in Fig. 7 and compared with the DNS and experimental data. The measurements of circumferential velocity fluctuations from PIV and LDA are not available. Use of both coarse grids resulted in overprediction of u_{rms} and underprediction of $u_{r_{\mathrm{rms}}}$ and $u_{\theta_{\mathrm{rms}}}$. For the fine grid, good agreement was achieved near the wall region, but both DNS and LES data underpredicted the u_{rms} near the core region. According to

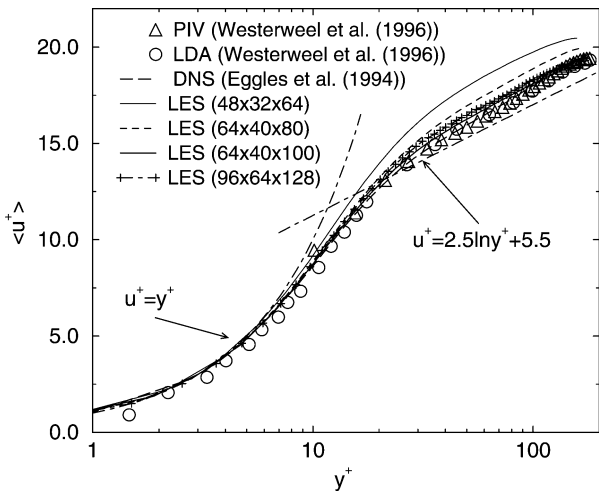

Fig. 6. Mean streamwise velocity profile in wall coordinates.

Table 1
Control volume dimensions in streamwise and radial directions

Grid	Streamwise spacing		Radius spacing			
	Δx	Δx^+	$\Delta r_{\min}$	$\Delta r^+_{\min}$	$\Delta r_{\max}$	$\Delta r^+_{\max}$
$48\times32\times64$	0.208	34.715	0.0087	1.45	0.0539	8.981
$64\times40\times80$	0.1563	26.955	0.0063	1.087	0.0446	7.694
$64\times40\times100$	0.1563	27.85	0.0063	1.123	0.0446	7.948

Table 2
Control volume dimensions in circumferential direction

Grid	Circumferential spacing			
	$(r\Delta\theta)_{\min}$	$(r\Delta\theta)^+_{\min}$	$(r\Delta\theta)_{\max}$	$(r\Delta\theta)^+_{\max}$
$48\times32\times64$	0.0053	0.8818	0.0982	16.359
$64\times40\times80$	0.0035	0.6038	0.0785	13.549
$64\times40\times100$	0.0028	0.4994	0.0628	11.197

Table 3
Mean flow properties of LES, DNS and experiments

	LES(coarser)	LES(coarse)	LES(fine)	DNS	PIV	LDA
$Re_\tau = u_\tau D/\nu$	333	345	356	360	366	371
u_b/u_τ	15.9	15.36	14.86	14.73	14.88	14.68
u_c/u_τ	20.47	19.95	19.14	19.31	19.38	19.39

Tennekes and Lumley [26], the turbulent intensities should drop to about $0.8u_\tau$ in the core region which is evident in the present rms profiles.

The skewness and flatness factors for the velocity fluctuations are shown in Figs. 8 and 9, respectively. The differences between the LES and DNS results and experiments were larger than for the second-order statistics; however, reasonable overall agreement between the present data and DNS and experimental statistics was obtained.

In Fig. 10, the one-dimensional wavenumber spectra of the streamwise and radial fluctuation velocities obtained from fine LES results are compared with the PIV data. Both the experimental and LES spectra are normalized by the corresponding rms values. In the wave number range from 5 to 20, the difference between LES and PIV is small except for the streamwise velocity fluctuations near the wall. This large discrepancy was also observed in the DNS results [1] and was explained to be most likely caused by a short simulation domain.

The shear stress contributions were calculated by

$$\tau_{\text{res}} = -\langle \rho u' u'_r \rangle, \tag{44}$$

$$\tau_{\text{vis}} = -\left\langle \frac{\mu}{Re}\frac{\partial u}{\partial r} \right\rangle, \tag{45}$$

$$\tau_{\text{SGS}} = -\left\langle \mu_t \frac{\partial u}{\partial r} \right\rangle, \tag{46}$$

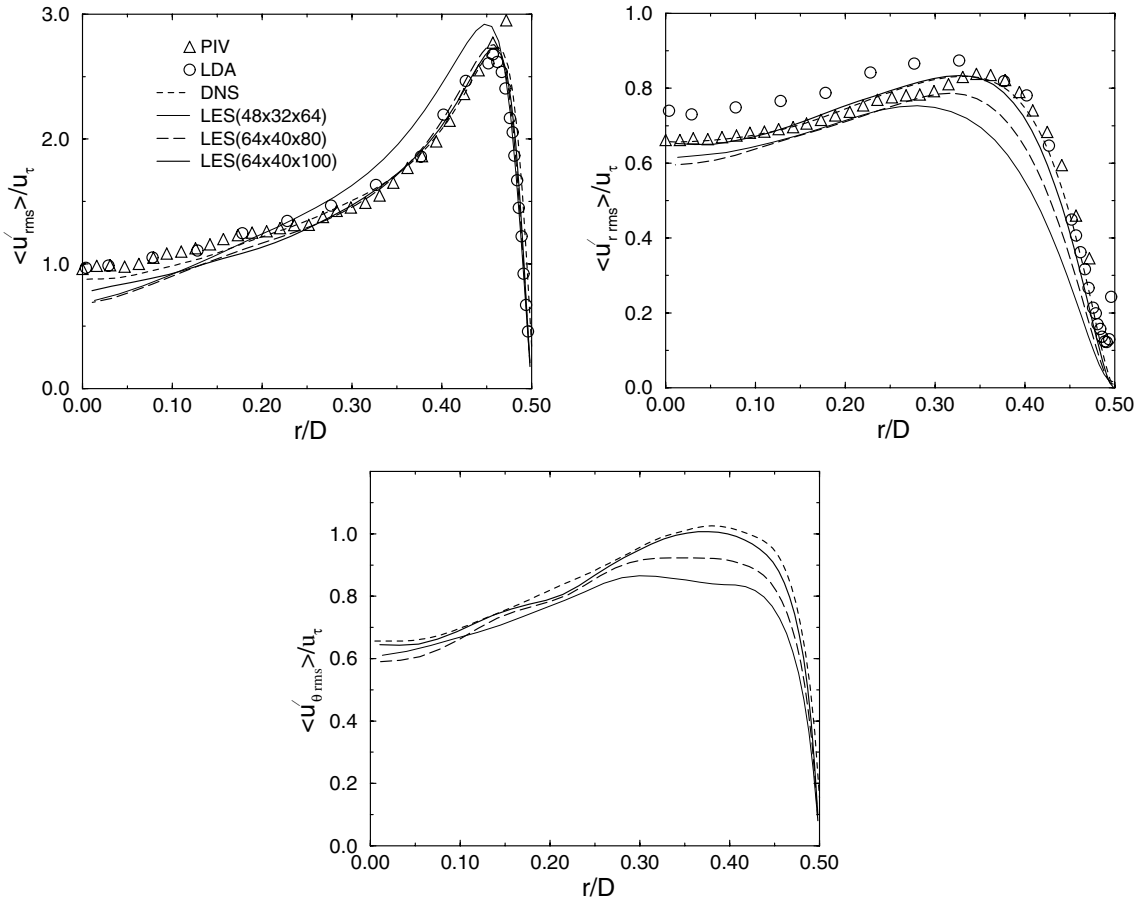

Fig. 7. RMS velocity fluctuations normalized by wall friction velocity.

where τ_{res} is the resolved Reynolds shear stress, τ_{vis} is the viscous shear stress, and τ_{SGS} is the modeled SGS stress. The shear stress contributions are shown in Fig. 11. The viscous shear stress is small near the core region and hence the Reynolds shear stresses with all three grid resolutions is similar near the core region. The viscous shear stress becomes important near the wall and the different Reynolds shear stress distributions are induced by the different grid resolutions. As shown, the coarse grids gave underprediction of the resolvable Reynolds shear stress and overprediction of the viscous shear stress near the wall. No DNS or experimental data are available for the modeled SGS stress. In the present simulations, the profiles of Reynolds shear stress and the viscous shear stress with the fine grid matched very well with the DNS and experimental data, while the coarse grids resulted in larger modeled SGS stress than the fine grid in the near wall region due to a larger value of the modeled SGS viscosity. Fig. 12 shows the ratio of the modeled SGS viscosity to the molecular viscosity for the three grids employed. This ratio is larger for coarser grids and the resulting level of dissipation may have been responsible for the overprediction of u_{rms} and the underprediction of $u_{r_{rms}}$ and $u_{\theta_{rms}}$ shown in Fig. 7.

The sum of the three shear stress contributions is the total shear stress and is shown in Fig. 13. Since the flow is fully developed and in a statistical steady state, the total shear stress must be linear, which is observed in the present simulations. It should be noted here that the linear distribution is independent of

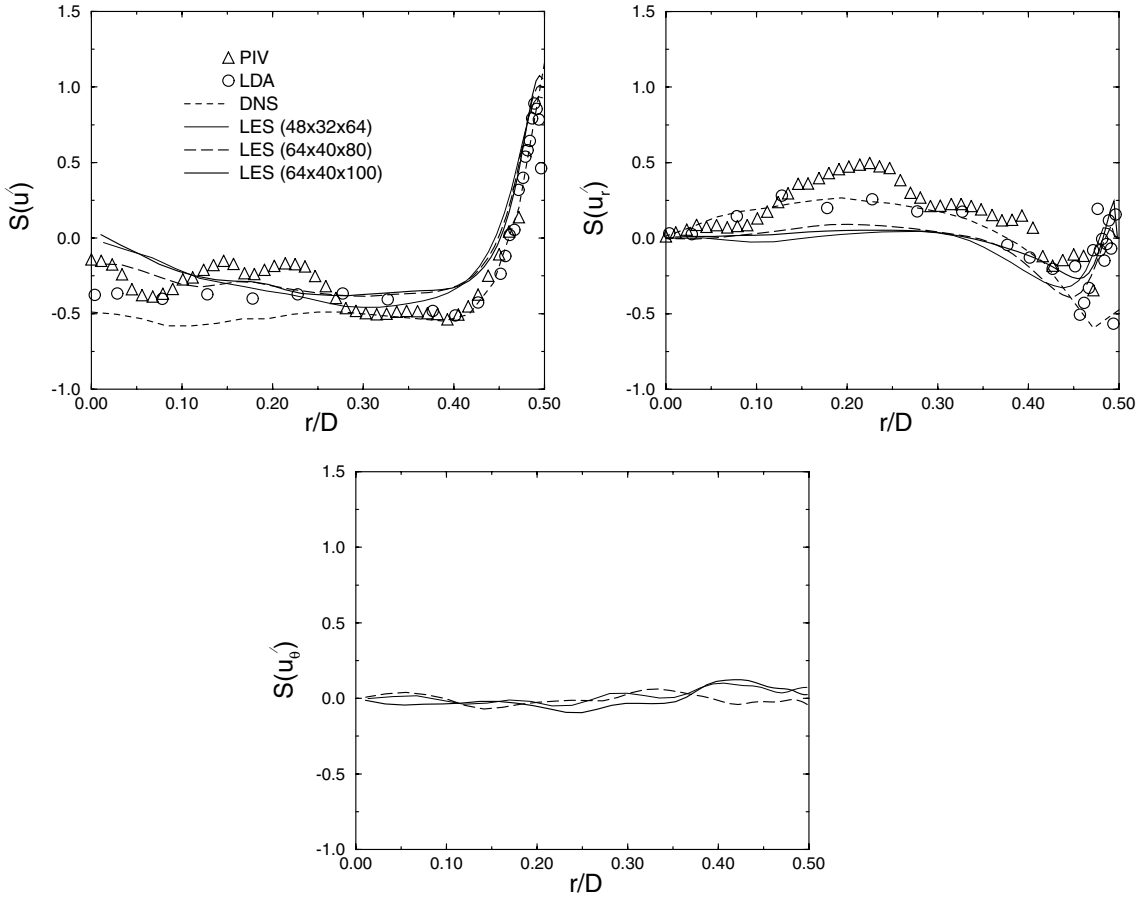

Fig. 8. Skewness factor of the velocity fluctuations.

the grids, because the normal-to-the-wall gradient of total shear stress must balance the pressure gradient, which is a fixed value for the fully developed flow.

As shown in Table 4, the average friction coefficient C_f obtained with the fine grid agrees well with the DNS results and experimental data. In the table, the difference between present results and the DNS or experimental data, diff, is defined as

$$\text{diff} = \frac{\text{present result} - \text{comparison data}}{\text{comparison data}}. \tag{47}$$

5.2. Coarse DNS results

The simulation without a SGS model was conducted to test effects of the SGS model. The same fine grid resolution, $64 \times 40 \times 100$, as for the LES was used, and the results which literally corresponded to coarse DNS results were compared with the LES results. As shown in Fig. 14, the mean streamwise velocity profile of this coarse DNS is very similar as the LES counterpart; however, a discrepancy in the rms values of the fluctuating velocities is observed in Fig. 15. LES predicted a larger peak value of u_{rms} which agreed better

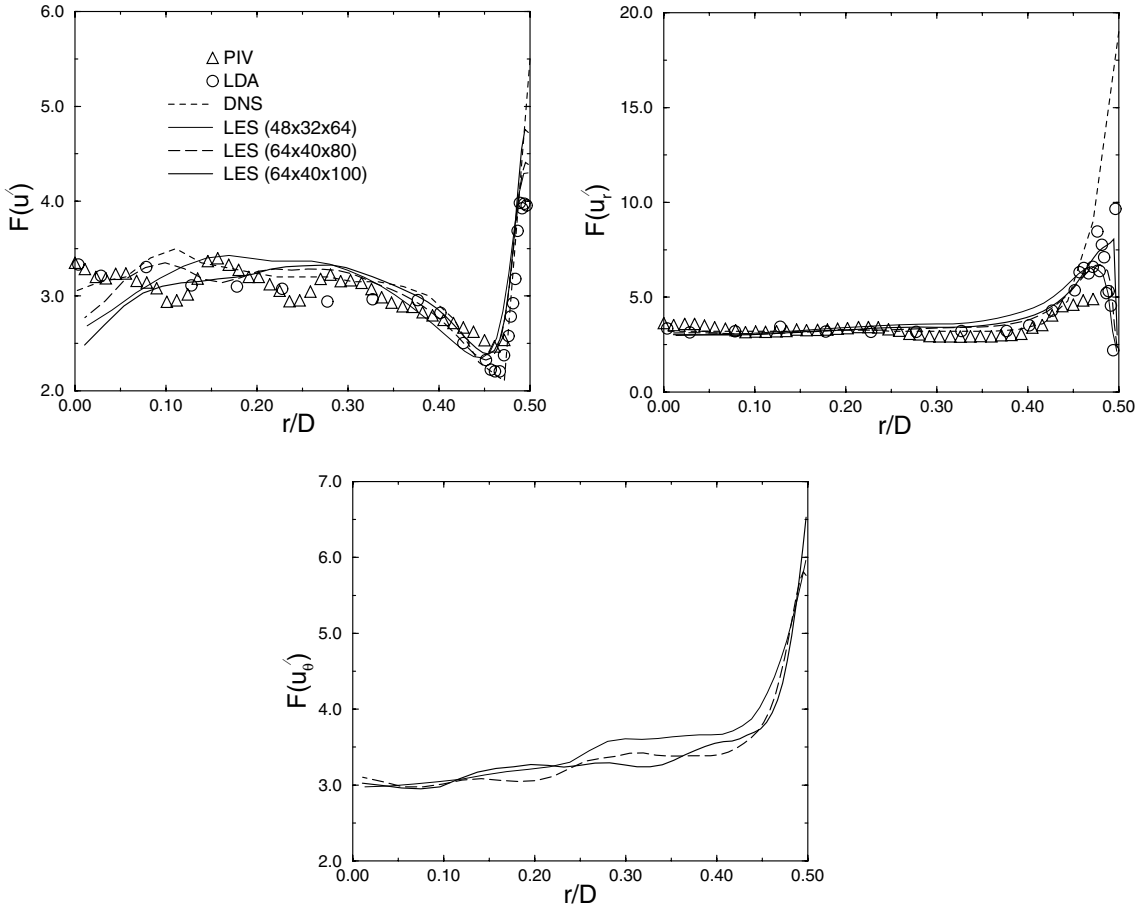

Fig. 9. Flatness factor of the velocity fluctuations.

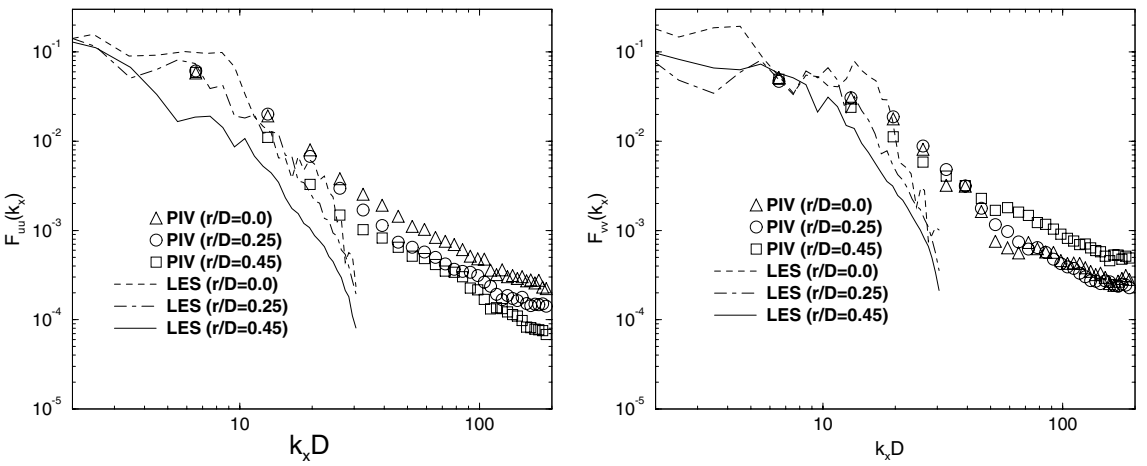

Fig. 10. Comparison of one dimensional wavenumber spectra of the fluctuating velocities between LES (fine) and PIV.

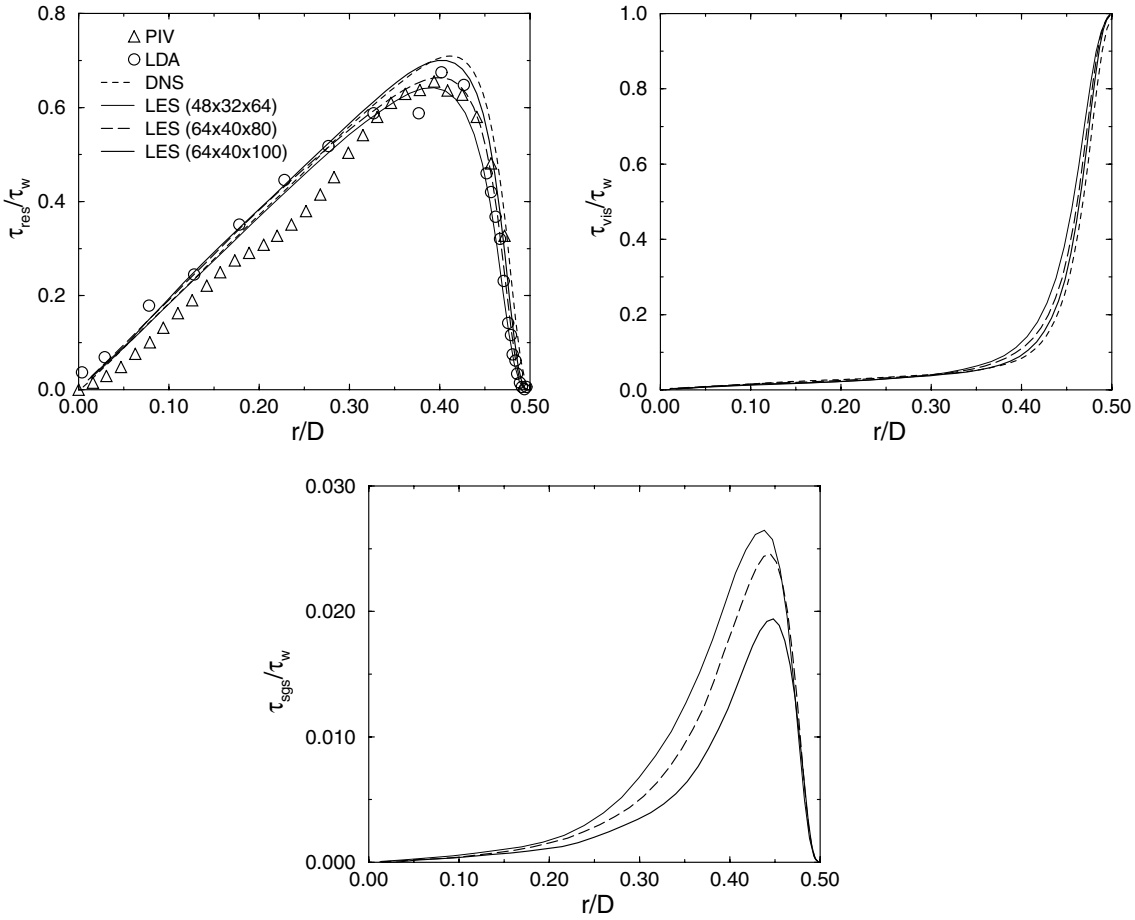

Fig. 11. Shear stress distributions scaled by wall shear stress.

with the DNS results [1] than did the coarse DNS results. The $u_{r_{\mathrm{rms}}}$ and $u_{\theta_{\mathrm{rms}}}$ profiles of the LES also matched with DNS results better than coarse DNS.

Since the Reynolds number of the current simulation is low, the finest LES grid resolution ($64 \times 40 \times 100$) may be sufficient to resolve most energy-carrying scales. Also the existing numerical dissipation will play the same role as the eddy viscosity to dissipate the turbulent energy. As a consequence, the coarse grid results deviated only slightly from the LES results. However, the comparison indicated that the additional dissipation added by the SGS model improved the results. Therefore, the current scheme has relative small numerical dissipation so that the dynamic SGS model plays an important role.

5.3. A simulation at a higher Reynolds number

Although this compressible LES formulation is most economical for applications to low Reynolds number turbulent pipe flows with significant property variations, a test for the capability of this LES scheme at higher Reynolds number was also conducted by simulating a fully developed turbulent pipe flow at the bulk Reynolds number of 20,000. The grid resolution was $96 \times 64 \times 128$ and the control volume dimensions in

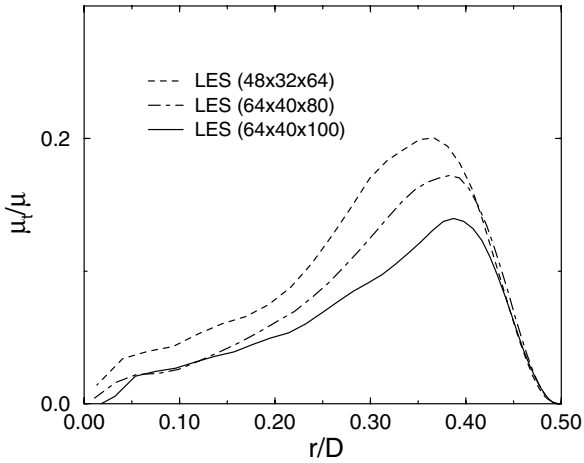

Fig. 12. Ratio between modeled SGS turbulent viscosity and molecular viscosity.

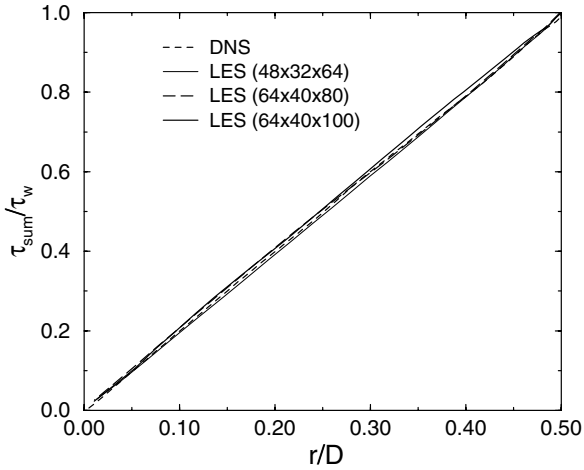

Fig. 13. Total shear stress distribution scaled by wall shear stress.

Table 4
Comparison of friction coefficient with $64 \times 40 \times 100$ grid

Correlation	C_f	Diff. (%)
Present simulation	0.00905	–
DNS	0.00922	−1.8
PIV	0.00903	+0.2
LDA	0.00928	−2.5

wall units are listed in Table 5. The simulation was run on an Alpha EV6.7 cluster using 8 processors, and required 12.6 CPU hours per processor per 1000 physical time step.

The results were compared with the available experimental data [27] obtained by using a single-component laser-Doppler velocimetry (LDV). As observed in Figs. 16–18, good agreement with experimental data

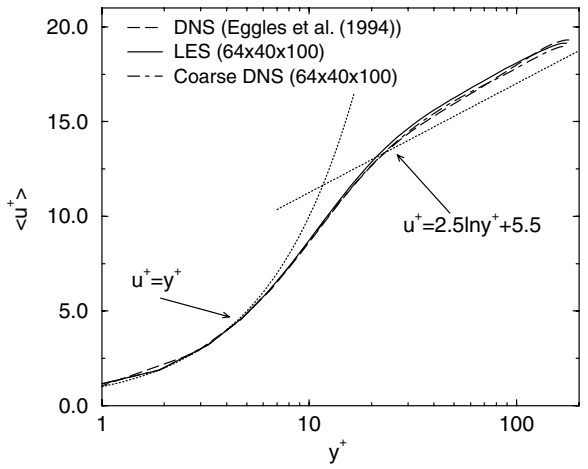

Fig. 14. Comparison of mean streamwise velocity profile in wall coordinates between coarse DNS and LES.

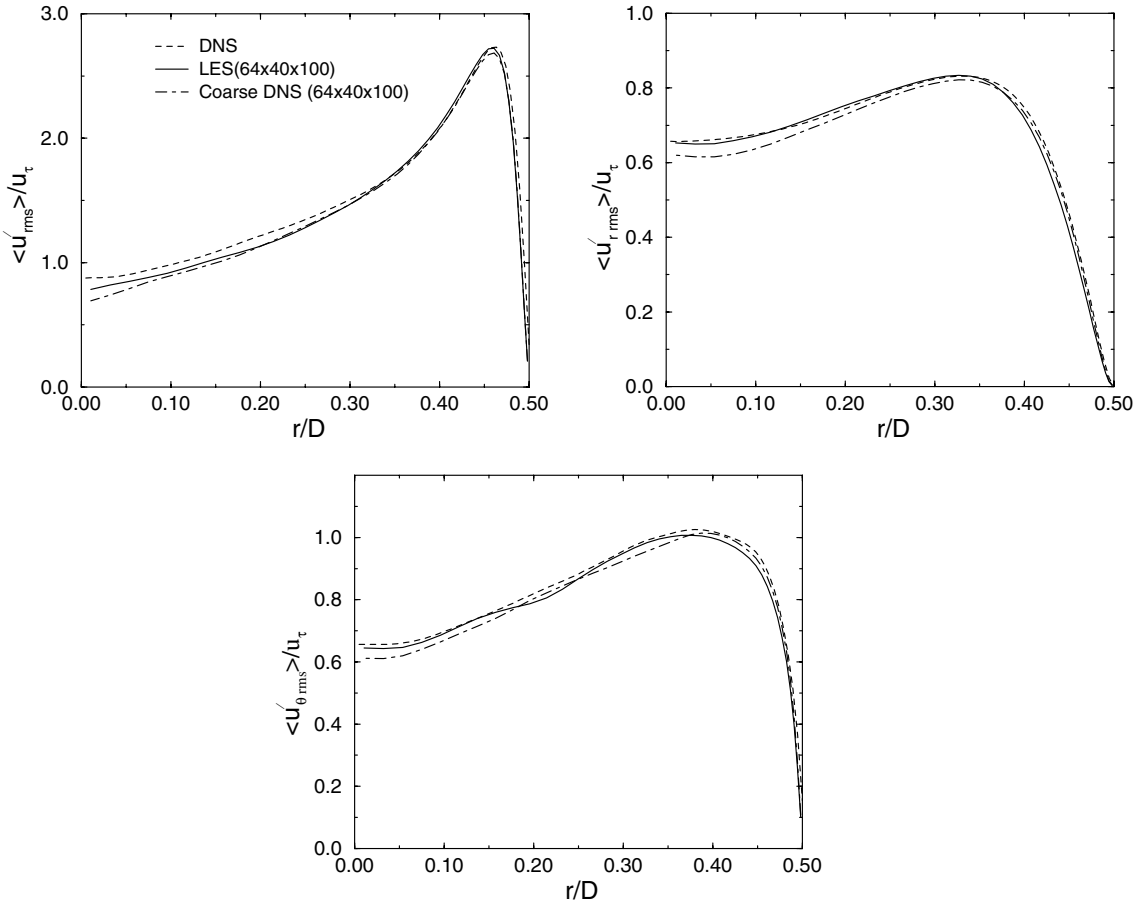

Fig. 15. Comparison of RMS velocity fluctuations normalized by wall friction velocity between coarse DNS and LES.

Table 5
Control volume dimensions in wall units

Δx^+	Δr^+_{min}	Δr^+_{max}	$(r\Delta\theta)^+_{min}$	$(r\Delta\theta)^+_{max}$
27.41	1.59	15.82	0.78	25.83

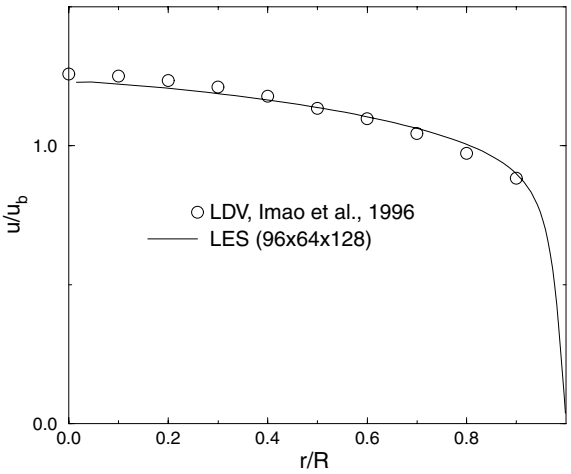

Fig. 16. Comparison of mean streamwise velocity profile.

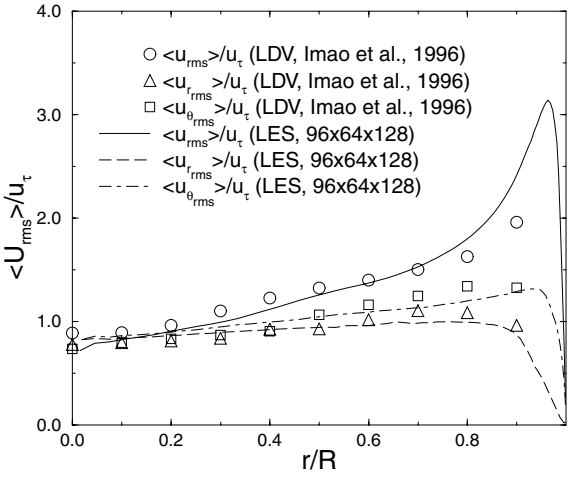

Fig. 17. Comparison of RMS velocity fluctuations.

were obtained, except a little underprediction was found for the rms values of fluctuating velocities in the radial and circumferential directions.

5.4. Turbulent pipe flow with very low heat transfer

To be continuing with the validation of the LES formulation for heat transfer, a low heat flux case was simulated to keep the effects of property variations small enough to allow comparison with passive scalar

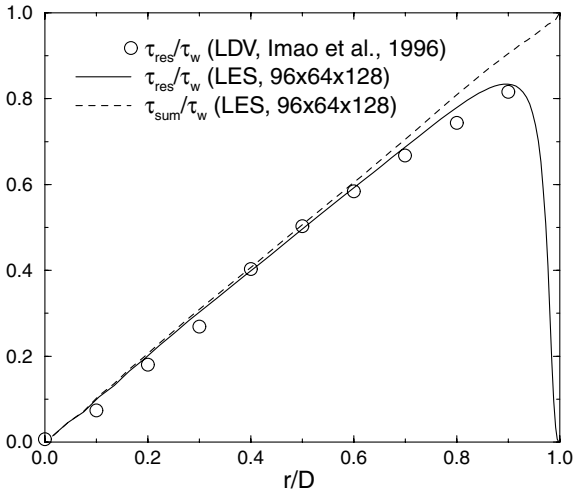

Fig. 18. Distribution of Reynolds shear stress and total shear stress profiles.

DNS heat transfer results. The configuration is shown in Fig. 19. The computational domain was the same as that used in isothermal turbulent pipe flow simulations and the fine grid resolution, $64 \times 40 \times 100$ grid in streamwise, radial and circumferential directions, was used.

For fully developed turbulent pipe flow with constant fluid properties, the time averaged streamwise velocity and temperature no longer change in the streamwise direction. Consequently, the average local, wall, and bulk streamwise temperature gradients are all equal to a constant and only depend on the amount of heat being added to the flow, as

$$\frac{\partial T}{\partial x} = \frac{\partial T_{\mathrm{w}}}{\partial x} = \frac{\partial T_{\mathrm{b}}}{\partial x} = \text{constant}, \tag{48}$$

where the bulk temperature is defined as

$$T_{\mathrm{b}} = \frac{1}{\rho_{\mathrm{b}} u_{\mathrm{b}} A_{\mathrm{c}}} \int \rho u T \, \mathrm{d}A. \tag{49}$$

Eq. (48) could be used in the current simulation because the flow was assumed to be quasi-developed and the property variations were very small. By setting a constant q_{w} value at the wall, the isoflux thermal boundary condition at the wall can be implemented by using Eq. (35). However, Kasagi et al. [28] and

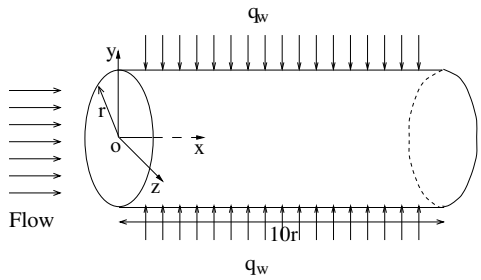

Fig. 19. Schematic of pipe flow with constant wall heat flux, q_{w}.

Dailey [13] reported that implementing the above condition for DNS and LES gives near wall fluctuations larger than observed experimentally because the simulations do not take into account the heat capacity of the wall. The wall temperature fluctuations should be negligibly small so that the wall could be regarded as isothermal.

In order to obtain small wall temperature fluctuations and achieve the desired heat flux, an alternative thermal boundary condition has also been investigated by setting a fixed wall temperature which varied linearly in the streamwise direction as follows:

$$T_{\mathrm{w}}(x) = T_{\mathrm{w}}(0) + \left(\frac{\partial T_{\mathrm{w}}}{\partial x}\right)x, \tag{50}$$

where $T_{\mathrm{w}}(0)$ is the wall temperature at the first location of simulating domain, and $\partial T_{\mathrm{w}}/\partial x$ is the wall temperature gradient along the streamwise direction. For nearly fully developed flow, the wall temperature gradient can be related to the specified heat flux. This fixed wall temperature distribution boundary condition was also used by Satake and Kunugi [29] in their DNS study.

The simulation was designed to compare with the passive scalar results of Satake and Kunugi [29], in which the non-dimensional DNS computational domain was $15 \times 1 \times 2\pi$ with a grid of $256 \times 128 \times 128$ points in the streamwise, radial, and circumferential directions, respectively. The non-dimensional wall heating rate was set as

$$q_{\mathrm{w}} = \frac{q^*_{\mathrm{w}}}{\rho_{\mathrm{ref}} U_{\mathrm{ref}} T_{\mathrm{ref}} C^*_{\mathrm{p}}} = 4.0 \times 10^{-4}. \tag{51}$$

The reference Mach number was set as $M_{\mathrm{ref}} = 0.001$ to ensure nearly incompressible results and the non-dimensional time step was 0.01.

The dimensionless temperature parameter, θ^+, is defined as

$$\theta^+(x, y, z, t) = \frac{\langle T^*_{\mathrm{w}}\rangle(x) - T^*(x, y, z, t)}{T^*_\tau}, \tag{52}$$

where $\langle T^*_{\mathrm{w}}\rangle$ is the averaged wall temperature and T^*_τ is the friction temperature. The friction temperature was calculated by

$$T^*_\tau = \frac{q^*_{\mathrm{w}}}{\rho^*_{\mathrm{w}} c^*_{\mathrm{p}} u^*_\tau}. \tag{53}$$

For the present simulations, the very low heat flux resulted in a wall-to-bulk temperature ratio of $T_{\mathrm{w}}/T_{\mathrm{b}} = 1.08$. Since the variation of the temperature parameter, θ^+, in the streamwise direction was negligibly small due to very low heat transfer, the ensemble averages of the temperature statistics were performed in the streamwise and circumferential directions and in time. The mean temperature profiles are plotted in wall coordinates in Fig. 20. The linear profile, $\theta^+ = Pry^+$, is matched exactly in the conductive sublayer with both isoflux and fixed linear wall temperature gradient thermal boundary conditions. The results also agree well with DNS data and the empirical log-law ($\theta^+ = 2.853 \ln y^+ + 2.347$) formula in the logarithmic region except for a little underprediction near the center.

The rms of the temperature fluctuations in the near wall region is shown in Fig. 21. The isoflux thermal boundary condition results in a large overprediction when compared with the DNS results, and unrealistically large temperature fluctuations at the wall. However, the rms temperature fluctuations obtained with fixed wall temperature distribution boundary condition match with the DNS data very well in the near wall region.

The streamwise and wall-normal turbulent heat fluxes normalized by friction velocity and temperature are shown in Figs. 22 and 23, respectively. A large overprediction of streamwise turbulent heat flux is

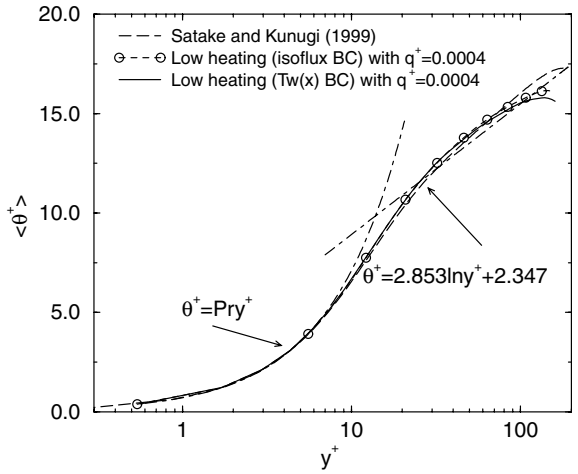

Fig. 20. Mean temperature distribution in wall coordinates for very low heat flux case.

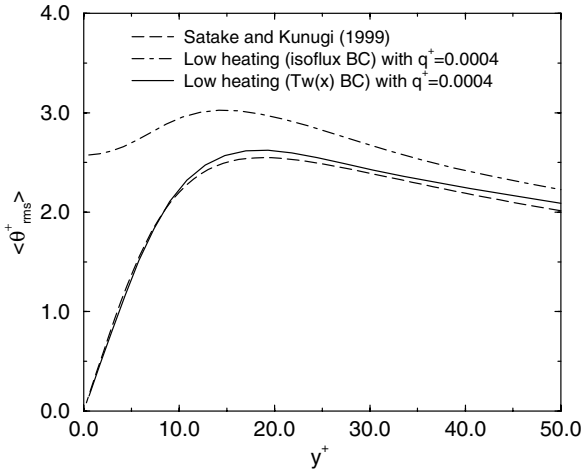

Fig. 21. RMS of the temperature fluctuations normalized by friction temperature.

observed for the isoflux thermal boundary condition, while very good agreement is obtained with the fixed wall temperature distribution boundary condition. It should be noted that although the temperature fluctuations do not agree very well with the DNS results in the core region of the pipe, fairly good agreement is obtained for the turbulent heat fluxes between the present simulations and DNS data. This good agreement may be because the velocity fluctuations dominated the temperature fluctuations here.

The ratios of the modeled SGS turbulent viscosity to the local molecular viscosity for the low heat transfer cases are plotted in Fig. 24. Because the molecular viscosity becomes larger and turbulence intensities become smaller in heat transfer cases, smaller values of $\mu_t/\mu(y)$ were observed compared with the isothermal case shown in Fig. 12.

The friction coefficients and Nusselt numbers for the present simulations with two different thermal boundary conditions are compared with the constant property correlations which were proposed by Gnielinski [30] and valid for $2300 < Re_D < 5 \times 10^6$. The friction coefficient correlation is

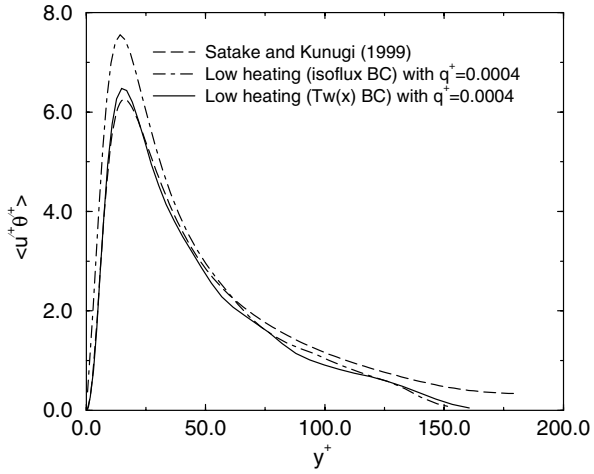

Fig. 22. Streamwise turbulent heat flux normalized by friction velocity and temperature.

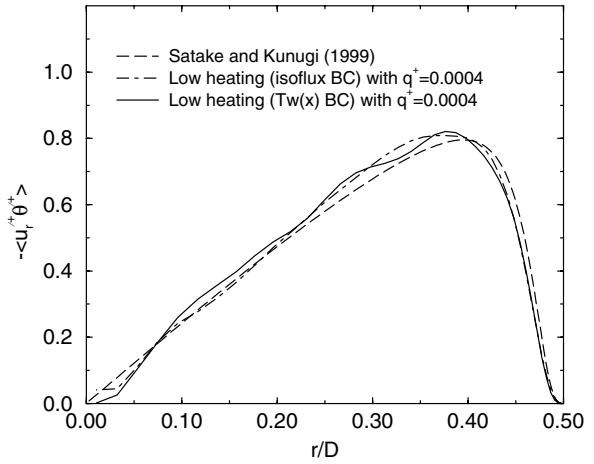

Fig. 23. Wall-normal turbulent heat flux normalized by friction velocity and temperature.

$$C_f = (1.58 \ln Re_D - 3.28)^{-2} \tag{54}$$

and the Nusselt number correlation is defined as

$$Nu_D = \frac{(C_f/2)(Re_D - 1000)Pr}{1 + 12.7(C_f/2)^{1/2}(Pr^{2/3} - 1)}, \tag{55}$$

where Re_D is the bulk Reynolds number based on hydraulic diameter. As shown in Table 6, the friction coefficient is overpredicted and Nusselt number is underpredicted when specifying the constant heat flux, q_w, value at the wall. It is observed from Table 7 that both friction coefficient and the Nusselt number are underpredicted compared with the correlation when the fixed wall temperature distribution boundary condition is used. Compared to the isothermal case, a slightly larger difference between the present simulations and correlations were observed, but agreement is still within the uncertainty band usually ascribed

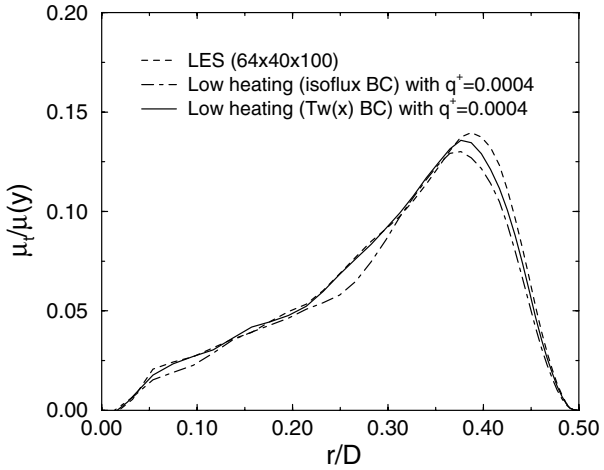

Fig. 24. Ratio between modeled SGS turbulent viscosity and local molecular viscosity for case with heat transfer.

Table 6
Comparison to constant property correlations with constant q_w

Correlation	C_f	Diff. (%)	Nu_D	Diff (%)
Present simulation (constant q_w)	0.01	–	16.3	–
Gnielinski (1976)	0.0095	+4.75	17.23	−5.4

Table 7
Comparison to constant property correlations with fixed T_w distribution

Correlation	C_f	Diff. (%)	Nu_D	Diff. (%)
Present simulation (fixed T_w)	0.0085	–	17.0	–
Gnielinski (1976)	0.0093	−8.6	18.0	−5.4

to the correlations for turbulent flows with heat transfer. The larger difference is most likely because the properties are not exactly constant in the present simulations.

6. Conclusions

In this study, a compressible finite volume scheme was developed based on conservation equations in Cartesian coordinates for the large eddy simulation (LES) of turbulent pipe flows with significant property variations using hexahedral and tetrahedral non-Cartesian control volumes. The algorithm solved the compressible Favre filtered Navier–Stokes equations in a fully coupled manner with a time-accurate implicit LU-SGS scheme. A time-derivative preconditioning technique was employed to enable the computation of nearly incompressible flows.

The second-order accurate finite volume LES formulation was first evaluated by simulating isothermal turbulent pipe flows at two Reynolds numbers. A grid dependence study was performed for the low

Reynolds turbulent flow which indicated that a grid resolution of $64 \times 40 \times 100$ in the streamwise, radial and circumferential directions was necessary and sufficient to produce satisfactory results. With this grid, very good agreement with DNS and experimental data were obtained for mean velocities, rms velocity fluctuations, and shear stress distributions. The overall agreement with DNS and experimental high-order statistics was reasonable. For frictions coefficient, excellent agreement was obtained with DNS and experimental data. Good agreement with experimental data was also obtained when simulating a turbulent pipe flow at a higher Reynolds number of 20,000.

The finite volume scheme was further evaluated by simulating turbulent pipe flows with low constant wall heat flux so that comparisons could be made with the passive scalar results. Two ways of imposing the uniform heat flux wall boundary conditions were investigated. The temperature statistics were compared with DNS passive scalar results. The mean temperature matched with DNS data very well with both boundary conditions. In the near wall region, the temperature fluctuations compared well with DNS results for the fixed wall temperature boundary condition, while it was overpredicted with constant q_w boundary condition. Good agreement was obtained with fixed wall temperature boundary condition in the near wall region for the turbulent heat fluxes. The friction coefficients and Nusselt numbers agreed to within the uncertainty band with the constant property empirical correlations.

The study indicated that the present second-order accurate finite volume formulation based on Cartesian coordinates is capable of performing accurate LES for the flow through pipe using hexahedral and tetrahedral control volumes with moderate grid resolution. The isoflux thermal boundary condition can be implemented by specifying a fixed temperature distribution at the wall and this boundary condition can be used to predict turbulent pipe flows with property variations.

Acknowledgement

The authors are grateful to the Department of Energy for support through grant DE-FG03-995F21924 under the NERI program. The authors would also like to acknowledge many helpful suggestions made by Dr. D. M. McEligot of Idaho National Engineering and Environmental Laboratory. Iowa State High Performance Computing Center and University of Minnesota Supercomputing Institute provided computational resources needed for this research.

References

[1] J.G.M. Eggels, F. Unger, M.H. Weiss, J. Westerweel, R.J. Adrian, R. Friedrich, F.T.M. Nieuwstadt, Fully developed turbulent pipe flow: a comparison between direct numerical simulation and experiment, J. Fluid Mech. 268 (1994) 175.
[2] P. Orlandi, M. Fatica, Direct numerical simulation of turbulent flow in a pipe rotating about its axis, J. Fluid Mech. 343 (1997) 43.
[3] S. Satake, T. Kunugi, Direct numerical simulation of turbulent pipe flow, Trans. JSME (in Japanese) 64–617B (1998) 65.
[4] S. Satake, T. Kunugi, Direct numerical simulation of an impinging jet into parallel disks, Int. J. Numer. Methods Heat Fluid Flow 8 (1998) 768.
[5] S. Satake, T. Kunugi, Direct numerical simulation of turbulent pipe flow with non-uniform surface heat flux, Thermal Sci. Eng. (in Japanese) 6 (2) (1998) 1.
[6] S. Satake, T. Kunugi, Direct numerical simulation of turbulent heat transfer in an axially rotating pipe flow: Reynolds stress and scalar-flux budgets, Bull. Am. Phys. Soc. 43 (1998) 1976.
[7] F. Unger, R. Friedrich, Large eddy simulation of fully-developed pipe flow, in: L.H. Hirschel (Ed.), Flow Simulations of High Performance Computers 1, NNFM, 38, 1993, p. 201.
[8] J.G.M. Eggles, F.T.M. Nieuwstadt, Large-eddy simulation of turbulent flow in an axially rotating pipe, in: Proceeding of the 9th Symposium on Turbulent Shear flows, 1993, pp. 310–1.
[9] B.J. Boersma, F.T.M. Nieuwstadt, Large-eddy simulation of turbulent flow in a curved pipe, Trans. ASME 118 (1996) 248.
[10] Z.-Y. Yang, Large eddy simulation of fully developed turbulent flow in a rotating pipe, Int. J. Numer. Methods Fluids 33 (2000) 681.

[11] S. Satake, T. Kunugi, A. Mohsen Shehata, D.M. McEligot, Direct numerical simulation for laminarization of turbulent forced gas flows in circular tubes with strong heating, Int. J. Heat Fluid Flow 21 (2000) 526.
[12] R.H. Pletcher, K.-H. Chen, On solving the compressible Navier–Stokes equations for unsteady flows at very low Mach numbers, AIAA Paper, 1993, p. 3368.
[13] L.D. Dailey, Large eddy simulation of turbulent flows with variable property heat transfer using a compressible finite volume formulation, Ph.D. Thesis, Iowa State University, Ames, IA, 1997.
[14] J.H. Ferziger, M. Peric, Computational Methods for Fluid Dynamics, Springer, Berlin, 1996.
[15] S. Ghosal, P. Moin, The basic equations of the large eddy simulations of turbulent flows in complex geometry, J. Comput. Phys. 118 (1995) 24.
[16] A. Favre, Turbulence: space–time statistical properties and behavior in supersonic flows, Phys. Fluids 26 (1983) 2851.
[17] A.W. Vreman, B.J. Geurts, H. Kuerten, Subgrid-modeling in les of computational flow, Appl. Sci. Res. 54 (1995) 191.
[18] P. Moin, K. Squires, W. Cabot, S. Lee, A dynamic subgrid-scale model for compressible turbulence and scalar transport, Phys. Fluids A 3 (1991) 2746.
[19] D.K. Lilly, A proposed modification of the Germano subgrid-scale closure method, Phys. Fluids A 4 (1992) 633.
[20] K.-H. Chen, J.-S. Shuen, Three dimensional coupled implicit methods for spray combustion flows at all speeds, AIAA Paper, 1994, p. 3047.
[21] C. Benocci, A. Pinelli, The role of the forcing term in the large eddy simulation of equilibrium channel flow, in: W. Rodi, E.N. Ganic (Eds.), Engineering Turbulence Modeling and Experiments, New York, 1990, p. 287.
[22] J. Westerweel, J.G.T.H. Draad, van der Hoeven, J. van Oord, Measurement of fully-developed turbulent pipe flow with digital particle image velocimetry, Exp. Fluids 20 (1996) 165.
[23] V.C. Patel, M.R. Head, Some observations on skin friction and velocity profiles in fully developed pipe and channel flows, J. Fluid Mech. 38 (1969) 181.
[24] J. Laufer, The structure of turbulence in fully developed pipe flow, NACA Report, 1954, p. 1174.
[25] C.J. Lawn, The determination of the rate of dissipation in turbulent pipe flow, J. Fluid Mech. 48 (1971) 477.
[26] H. Tennekes, J.L. Lumley, A First Course in Turbulence, MIT Press, Cambridge, MA, 1972.
[27] Shigeki Imao and Motoyuki Itoh, Turbulent characteristics of the flow in an axially rotating pipe, Int. J. Heat Fluids Flow 17 (1996) 445.
[28] N. Kasagi, A. Kuroda, M. Hirata, Numerical investigation of near wall turbulent heat transfer taking into account the unsteady heat conduction in the solid wall, J. Heat Transfer 111 (1989) 53.
[29] S. Satake, T. Kunugi, Direct numerical simulation of turbulent pipe flow with uniform surface heat flux, Trans. JSME (in Japanese) 65-631B (1999) 192.
[30] V. Gnielinski, Neue gleichungen für den wärme- und den stoffübergang in turbulent durchströmenten rohren und kanalen, Int. Chem. Eng. 16 (1976) 359.